Automatic Mode Transition Enabled Robust Triboelectric Nanogenerators

Jun Chen,[†,∥] Jin Yang,[†,‡,∥] Hengyu Guo,[†] Zhaoling Li,[†] Li Zheng,[†] Yuanjie Su,[†] Zhen Wen,[†] Xing Fan,[*,†,§] and Zhong Lin Wang[*,†,⊥]

[†]School of Materials Science and Engineering, Georgia Institute of Technology, Atlanta, Georgia 30332-0245, United States, [‡]Department of Optoelectronic Engineering and [§]College of Chemistry and Chemical Engineering, Chongqing University, Chongqing 400044, China, and [⊥]Beijing Institute of Nanoenergy and Nanosystems, Chinese Academy of Sciences, Beijing 100083, China. [∥]J.C. and J.Y. contributed equally.

ABSTRACT Although the triboelectric nanogenerator (TENG) has been proven to be a renewable and effective route for ambient energy harvesting, its robustness remains a great challenge due to the requirement of surface friction for a decent output, especially for the in-plane sliding mode TENG. Here, we present a rationally designed TENG for achieving a high output performance without compromising the device robustness by, first, converting the in-plane sliding electrification into a contact separation working mode and, second, creating an automatic transition between a contact working state and a noncontact working state. The magnet-assisted automatic transition triboelectric nanogenerator (AT-TENG) was demonstrated to effectively harness various ambient rotational motions to generate electricity with greatly improved device robustness. At a wind speed of 6.5 m/s or a water flow rate of 5.5 L/min, the harvested energy was capable of lighting up 24 spot lights (0.6 W each) simultaneously and charging a capacitor to greater than 120 V in 60 s. Furthermore, due to the rational structural design and unique output characteristics, the AT-TENG was not only capable of harvesting energy from natural bicycling and car motion but also acting as a self-powered speedometer with ultrahigh accuracy. Given such features as structural simplicity, easy fabrication, low cost, wide applicability even in a harsh environment, and high output performance with superior device robustness, the AT-TENG renders an effective and practical approach for ambient mechanical energy harvesting as well as self-powered active sensing.

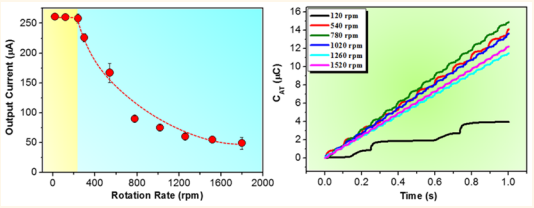

KEYWORDS: triboelectric nanogenerator · automatic transition · self-powered · speedometer

With the threatening of global warming and diminishing fossil fuel, searching for renewable and green energy resources with reduced carbon emissions is one of the most urgent challenges to the sustainable development of human civilization.[1−3] In the past decades, increasing research efforts have been committed to seek clean and renewable energy sources as well as to develop renewable energy technologies.[4−7] Mechanical motions, holding a wide range of scales with various forms, are abundant in ambient environment and people's daily life. In recent years, it has become an attractive target for energy harvesting as a promising supplement to traditional fuel sources and a potentially alternative power source for battery-operated electronics.

Recently, relying on the coupling effect of contact electrification and electrostatic induction, the triboelectric nanogenerator (TENG) has been invented as a fundamentally new and renewable energy technology in the field of mechanical energy harvesting,[8−13] featured as extremely low cost, with high-energy conversion efficiency, diversity in working modes, and extensive adaptability on structural design for various applications.[14−29] However, a requirement of surface friction between two contact materials for a decent output renders a common challenge for the TENGs, where material abrasion and the concomitantly generated heat can create the challenge of long-term continuous service for the devices, especially for the in-plane sliding mode of the TENG.[30−32] In this regard, a noncontact working mode of the TENG with a designed free-standing gap between two triboelectric layers was developed with largely improved device robustness. However, a low output performance and the unavoidable triboelectric charge dissipation placed an awkward dilemma in the way of the TENG toward practical applications.[33,34]

* Address correspondence to zhong.wang@mse.gatech.edu, foxcqdx@cqu.edu.cn.

Received for review September 7, 2015 and accepted November 3, 2015.

Published online 10.1021/acsnano.5b05618

Herein, we reported a rationally designed automatic transition triboelectric nanogenerator (AT-TENG) that is expected to be robust by, first, converting the in-plane sliding electrification into a contact separation working mode and, second, generating a rotation-speed-controlled automatic transition between a contact working state and a noncontact working state. A greatly reduced surface friction assures the drastically improved device robustness. Meanwhile, an intermittent transition into the contact state also resolved the awkward predicament of triboelectric charges dissipation in the noncontact free-standing mode, which assures a high electric output performance.

The AT-TENGs were demonstrated to efficiently harness various ambient mechanical motions for long-time continuous operation without any observable electrical output degradation. Due to the rational design with a fully enclosed structure, the AT-TENGs are also capable of performing adequately in harsh environmental conditions. At a wind speed of 6.5 m/s or a water flow rate of 5.5 L/min, the harvested energy was capable of lighting up 24 spot lights (0.6 W each) simultaneously and charging a capacitor up to 120 V in 60 s. Still, the AT-TENG was also developed to recycle the wasted rotational energy from bicycling and normal car motion, and the generated power was capable of lighting up 24 spot lights or 104 light-emitting diodes (LEDs) simultaneously. In addition, an AT-TENG-based self-powered speedometer was developed with ultrahigh measurement accuracy owing to its unique output characteristics. In a word, given such features as structural simplicity, easy fabrication, extremely low cost, wide applicability, and high output performance with superior device robustness, the AT-TENGs presented in this work provide a green and sustainable technology to convert ambient mechanical motions. It is a solid step for TENGs toward practical applications and will especially be widely adopted in wheel-based transport systems for either energy harvesting or self-powered sensing purposes.

RESULTS AND DISCUSSION

The device structure of an AT-TENG is schematically illustrated in Figure 1a, which mainly consists of two parts, a functional unit and a rotator. The functional unit has a multilayer structure with acrylic as a supporting substrate. Acrylic was selected as the structural material because of its decent strength, light weight, good machinability, and low cost.[35,36] The two triboelectric layers are laminated with a full contact at their initial states. One end of them is secured by a piece of rubber, while the other end stays open. On the top triboelectric layer, aluminum thin film with a nanoporous surface plays dual roles of an electrode and a contact surface. Scanning electron microscopy (SEM) image of the nanopores on the aluminum is presented in Figure 1b. On the bottom triboelectric layer, polytetrafluoroethylene (PTFE) film with deposited copper as the back electrode acted as another contact surface, and it was anchored onto the bottom substrate. A top-down method through reactive ion etching was employed to create PTFE nanowire arrays on the PTFE surface.[37] An SEM image of the PTFE nanowires is displayed in Figure 1c. Here, a pair of magnets were adhered onto the top triboelectric layer and the rotator plane with a same pole facing each other. It is worth noting that the functional unit of AT-TENG for electricity generation was fully enclosed, and its operation relies on the external rotator with a magnet. This novel structure design renders it capable of performing adequately under harsh environmental conditions. A detailed fabrication process of the AT-TENG is presented in the Methods section.

The fundamental working principle of the AT-TENG is based on a two-way coupling of contact electrification and electrostatic induction.[38−42] As presented in Figure 2, both two-dimensional potential distribution by COMSOL (up) and schematic illustrations of charge distribution (down) were employed to elucidate the working principle of the AT-TENG, in which two working states were depicted: contact working state (Figure 2a−c) and noncontact free-standing working state (Figure 2d−f).

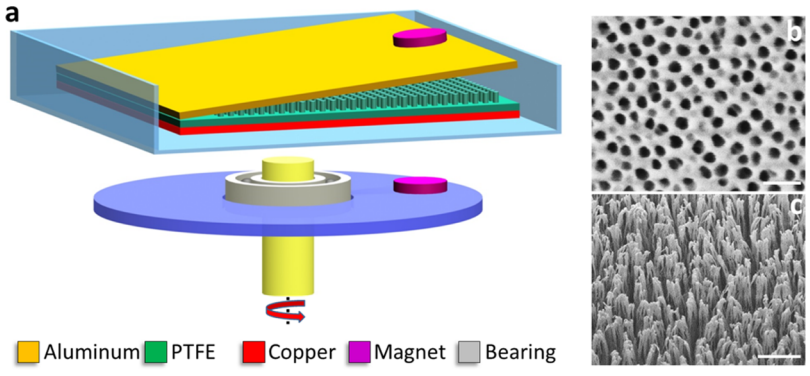

Figure 1. Structural design of the AT-TENG with one segment. (a) Schematic illustration of the triboelectric nanogenerator. (b) SEM image of the nanopores on an aluminum electrode. The scale bar is 150 nm. (c) SEM image of the PTFE nanowires. The scale bar is 500 nm.

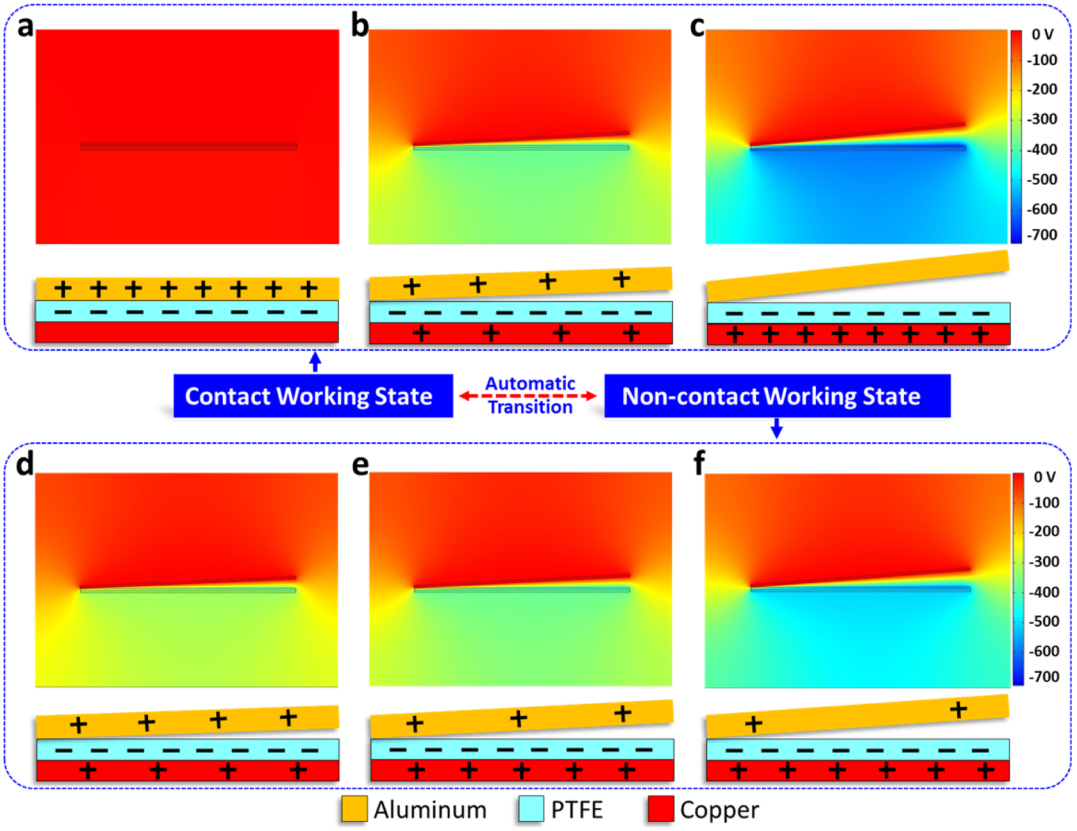

Figure 2. Schematics of the operating principle of the AT-TENG. Both two-dimensional potential distribution by COMSOL (up) and schematic illustrations of charge distribution (down) were employed to elucidate the working principle of the TENG. Two states were elucidated: (a−c) contact separation working state and (d−f) noncontact free-standing working state. (a) Initial state in which the PTFE is negatively charged after contact with aluminum. (b) Magnetic repulsion force separates the PTFE and aluminum. Electric potential difference drives the electrons from copper to aluminum, screening the triboelectric charges and leaving behind the inductive charges. (c) By continuously increasing the separation, all positive triboelectric charges are gradually and almost entirely screened. When the magnetic repulsion force disappears, the top aluminum plate will be dragged back to contact again with the PTFE. At a high rotation speed, another cycle of magnetic repulsion force will appear before the aluminum plate fully contacts the PTFE. Under such a circumstance, the AT-TENG works in a free-standing state, and the top aluminum will vibrate in a small range of separation distances with a high frequency. (d) Minimum separation distance. (e) Transition state moves upward to the maximum separation state. (f) Top aluminum is raised up to the maximum separation distance.

Regarding the contact working state, the aluminum is initially aligned and in full contact with PTFE (Figure 2a). According to the triboelectric series, PTFE is much more triboelectrically negative than aluminum, and electrons are injected from aluminum into PTFE,[43−45] generating positive triboelectric charges on the aluminum and negative ones on the PTFE. When the external rotation brings the paired magnets to meet, the repulsion force will push the two triboelectric layers apart. The induced electric potential difference drives the electrons to flow from copper to aluminum (Figure 2b), screening the triboelectric charges and leaving behind the inductive charges. The flowing of electrons will be continued until a maximum separation distance is reached, and all electrons are transferred from copper to aluminum (Figure 2c). The increased separation distance between the layers leads the weakened magnetic repulsive force; thus, the restoring force of the elastic and the gravity of the top triboelectric layer will pull it downward and back to contact with the lower triboelectric layer. This is a full cycle of the operation for the AT-TENG in the contact working state. The variation of electric potential regarding this state is visualized *via* COMSOL in Supporting Information Movie 1.

With a further increase of the rotation speed, the AT-TENG can transit to be in a noncontact free-standing working mode. At a higher rotation rate, the magnetic repulsive force has a shorter exertion time, which produces a much smaller momentum to the top triboelectric layer. Therefore, the top triboelectric layer will be pulled downward slightly due to the joining effect of centrifugal force and gravitation. Meanwhile, due to the fast rotation speeds, the top triboelectric layer will soon be magnetically repulsed again before it falls back into contact with the bottom triboelectric layer. As a consequence, the top triboelectric layer will vibrate around its equilibrium position at the frequency of the rotation, which will change the capacitance of the structure, resulting in an alternating

current across the electrodes. As shown in Figure 2d, when the top triboelectric layer falls to the lowest point at the minimum separation distance at a certain rotation rate, the electrons flowing from aluminum to copper will not fully screen the triboelectric charges in the copper electrode. When the repulsive force pushes the top triboelectric layer to move upward, the electrons will keep flowing from the copper to the aluminum (Figure 2e), until it reaches the highest point, corresponding to a maximum separation distance between the two (Figure 2f). Likewise, for a better view, the variation of the electric potential in the noncontact working state is also visualized *via* COMSOL in Supporting Information Movie 2.

To systematically investigate the performance of the AT-TENG as a new methodology in harvesting ambient mechanical energy, AT-TENGs with one segment and two segments were studied. For a better definition, Supporting Information Figure S1 gives a two-dimensional illustration of the two types of AT-TENGs. The fundamental working principle of the two-segment AT-TENG was also visualized *via* COMSOL in Supporting Information Movie 3. Figure 3a,b shows the dependence of the open-circuit voltage and short-circuit current, respectively, on the rotation rates for the one-segment AT-TENG. At a rotation rate less than 240 rpm, the one-segment AT-TENG is in a contact separation working state, and an open-circuit voltage up to 530 V is delivered, with which the short-circuit current shares the same trend and was stable around 0.26 mA. At this typical contact separation working stage, the open-circuit voltage can be estimated as

$$V_{oc} = \frac{\sigma d}{\varepsilon_o} \tag{1}$$

where ε_o is the vacuum permittivity and σ is the triboelectric charge density, d is the maximum separation of two triboelectric layers in an AT-TENG, which is designable and confined by the height of the device's external packaging. A detailed definition of d is presented in Supporting Information Figure S2. At a lower rotation rate, the AT-TENG works at the contact separation mode with a confined separation distance, which equates to d. This explained a constant electric output at current state.

By increasing the rotation rate beyond the critical point, the AT-TENG will be automatically converted from the contact working state into a noncontact freestanding working state. For each AT-TENG, the critical rotational speed is designable and can be estimated as follows (see Supporting Information for detailed derivation of the analytical model):

$$\omega_{crs} = \sqrt{\frac{\frac{F}{M}(\Delta\theta)^2 - 4\pi g(\Delta\theta - \pi)}{8d}} \tag{2}$$

where F is the magnetical repulsion force, M is the total weight of the top triboelectric layer, g is the gravitational acceleration, and $\Delta\theta$ is the field angle of the magnet on the rotator plane, which was determined by the magnet dimension. Based on the above analytical mode, it is safe to conclude that the critical rotational speed is highly correlated to a variety of parameters, including the weight of the top substrate, the height d of the external package, and the dimension and magnetism of the paired magnets.

As shown in Figure 3a,b, experimentally, the critical rotation rate of the as-fabricated AT-TENG with one segment is measured to be 240 rpm. Beyond it, the AT-TENG operates in a noncontact working state in a wide speed range up to 1800 rpm. In this stage, both the voltage and current amplitudes show a decreasing function of the rotation rate ω. Here, theoretically, the open-circuit voltage of the AT-TENG can be calculated as follows (see Supporting Information for detailed derivation of the analytical model):

$$V_{oc} = \left(\frac{\sigma}{\varepsilon_o}\right)\left(\frac{\frac{F}{M}(\Delta\theta)^2 - 4\pi g(\Delta\theta - \pi)}{8\omega^2}\right) \tag{3}$$

According to eq 3, in the noncontact working state, the output voltage is also related to various parameters, such as the weight of the top substrate, the dimension and magnetism of the paired magnets, and so on. Particularly, it is also inversely proportional to the square of rotation rate, which is consistent with the experimental observation.

For a systematical study of the presented methodology, the dependence of the open-circuit voltage and short-circuit current of the two-segment AT-TENG on the rotation rate was also investigated. As shown in Figure 3c,d, below the threshold rotation rate of 300 rpm, the two-segment AT-TENG was in a contact separation working state. In this stage, similar to the one-segment case, the voltage and current are constant at 246 V and 0.12 mA, respectively. The finite element simulation was also employed to theoretically study the open-circuit voltage of the two-segment AT-TENG, as presented in Supporting Information Figure S3. It shows a good consistency with the experimental results. With a further increase in the rotation rate beyond 300 rpm, the AT-TENG with two segments works in a noncontact freestanding mode, and the peak amplitudes of the electrical output decrease with an increase of the rotation rates, which shares the same trend as that with the one-segment AT-TENG. This is mainly attributed to the reduced separation distance between the two triboelectric layers of the AT-TENGs at higher rotation rates.

Here, it is worth noting that, for both one-segment and two-segment AT-TENGs, the reduced electric output amplitudes do not mean a reduction of the capability of the device for energy harvesting at higher rotation rates. First, as shown in Supporting Information Figures S4–S7, the peak density of the device's

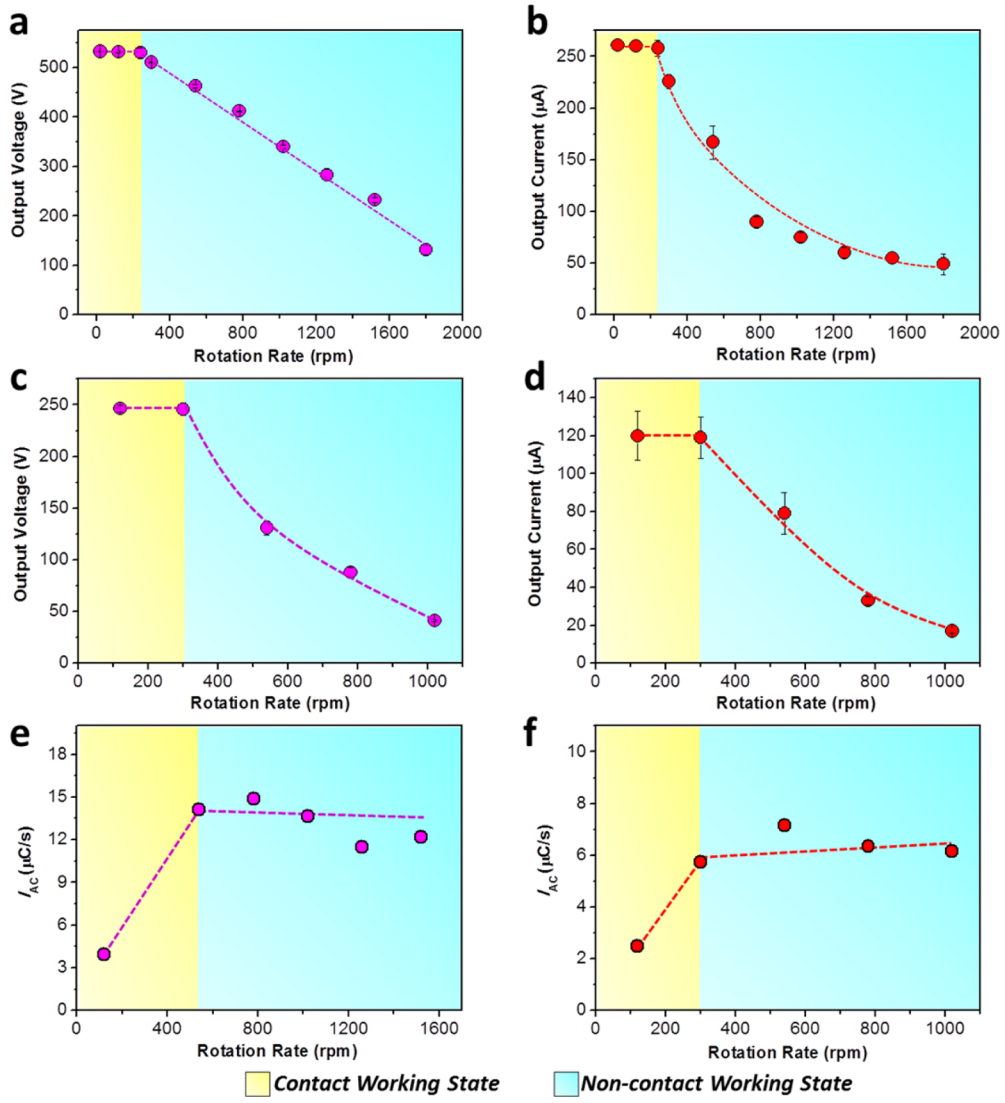

Figure 3. Electrical output characterization of the AT-TENGs. For a systematic investigation, two types of AT-TENGs, one-segment and two-segment, were studied. Dependence of the (a) open-circuit voltage and (b) short-circuit current on the rotation rate of the one-segment AT-TENG. Dependence of the (c) open-circuit voltage and (d) short-circuit current on the rotation rate of the two-segment AT-TENG. Dependence of the average charge transfer rates on the rotation rate for the (e) one-segment AT-TENG and (f) two-segment AT-TENG.

electric output is dramatically increased with the increased rotation rate. This leads to an increasing amount of the transferred triboelectric charges across the electrodes. The dependence of the average charge transfer rate (I_{AC}) on the rotation rates for the two types of AT-TENGs are presented in Figure 3e,f. Here, I_{AC} is defined as the total transferred charges across the electrodes per unit operation time. As shown, at higher rotation rates beyond the critical point, the devices are working at a noncontact state, and they are maintained at a charge transfer rate higher than that in the contact working state. As a consequence, the capability of the AT-TENG for energy harvesting is actually enhanced at higher rotation rates. Furthermore, the dependence of the accumulative transferred charges (C_{AT}) on the rotation rate for the two types of AT-TENGs was also measured and plotted in Figure 4a,b. Likewise, much higher C_{AT} values were maintained for the AT-TENG in the noncontact working state and especially at the rotation rates around the critical point or in the short-range above it.

Resistors were utilized as the external load to further investigate the output power of the AT-TENG around the critical rotation rate. As displayed in Figure 4d, the voltage amplitudes increase with the increasing of the load resistances, while the current amplitudes follow a reverse trend due to the ohmic loss, as presented in Supporting Information Figure S8. As a consequence, the instantaneous peak power is maximized at a load resistance of 1 MΩ, corresponding to a peak power density of 1 W/m^2. The superior robustness is also an advantageous feature of the reported AT-TENG. As shown in Figure 4d, there is no observable output degradation after 300 000 cycles of continuous operation

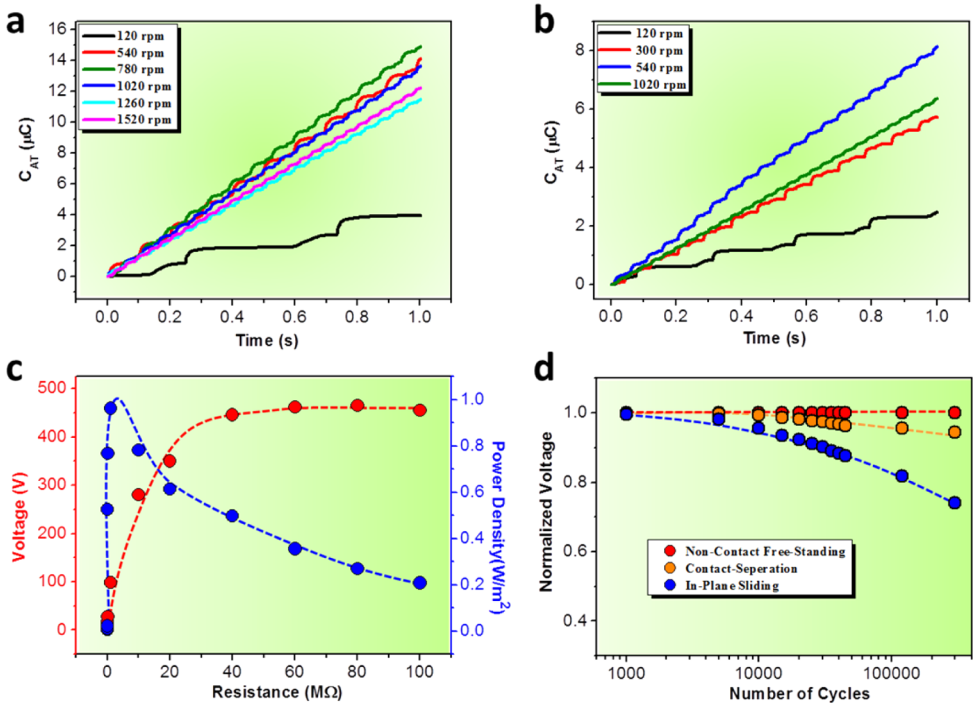

Figure 4. Accumulative transferred charges and the delivered power of the AT-TENGs. Dependence of the accumulative transferred charges across the electrodes on the rotation rate for (a) one-segment AT-TENG and (b) two-segment AT-TENG. (c) Dependence of the peak power output obtained at the external load resistances for the one-segment TENG at a rotation rate around 240 rpm, indicating maximum power output at $R = 1$ MΩ. (d) Working state dependent device robustness investigation.

when the AT-TENG operated in the noncontact free-standing working state, and a minor fluctuation of less than 6% was observed for the contact separation working mode. Notably, an obvious degradation up to 26% was observed for the in-plane sliding mode. On one hand, by converting the in-plane sliding electrification into the contact separation mode, the device robustness of the AT-TENG was greatly improved. On the other hand, as long as the AT-TENG works at its critical point or in the short-range above the critical point with an occasional transition into a contact state for charge replenishment, the AT-TENGs could pave a new way of keeping both high electric output and superior device robustness.

To prove it as a robust and sustainable energy technology, the AT-TENG was demonstrated to efficiently harness various ambient mechanical motions for long-time continuous operations. Here, a first step was taken to develop the AT-TENG into a wind energy harvester by equipping it with a wind cup. Figure 5a is a photograph of the as-fabricated device, and Figure 5b shows the device in the ambient environment. Drove by the light wind at a flow speed of 6.5 m/s, the harvested energy by the AT-TENG is capable of simultaneously lighting up an array of 24 spot lights (0.6 W each) connected in series (Figure 5c and Supporting Information Movie 4). Furthermore, the AT-TENG was also demonstrated to harvest energy from the environmental water flow. Figure 5d,f shows, respectively, the setup for water flow energy harvesting and the upward view of the water turbine employed. At a flow rate of 5.5 L/min *via* a water pipe, the harvested power can also be utilized to simultaneously light up an array of 24 spot lights connected in series (Figure 5e and Supporting Information Movie 5). Meanwhile, as shown in Figure 5g, the harvested energy from the wind and water flow by the AT-TENG was also capable of charging a commercial capacitor up to more than 120 V in 60 s. The AT-TENG was also further demonstrated to recycle mechanical energy from bicycling and a moving car. As shown in Figure 6a, an AT-TENG was equipped onto a commercial bicycle. An enlarged view of the installation is presented in Figure 6b. The harvested power is also capable of lighting up 24 spot lights simultaneously when a human rides a bike naturally (Supporting Information Movie 6). Still, the AT-TENG can also harvest energy from a moving car. As shown in Figure 6c and Supporting Information Movie 7, about 104 LEDs were lighted up simultaneously when a car was running at normal speed.

In addition, due to the unique output characteristics, the AT-TENG was also demonstrated to be a self-powered speedometer with ultrahigh measurement accuracy, which can measure not only the wheel moving speed but also the traveled distance in a real-time manner. Read the acquired electric signals from an *N*-segment AT-TENG, the rotational speed in rpm at this moment can be expressed as

$$R_t = 60/(N\Delta t) \quad (4)$$

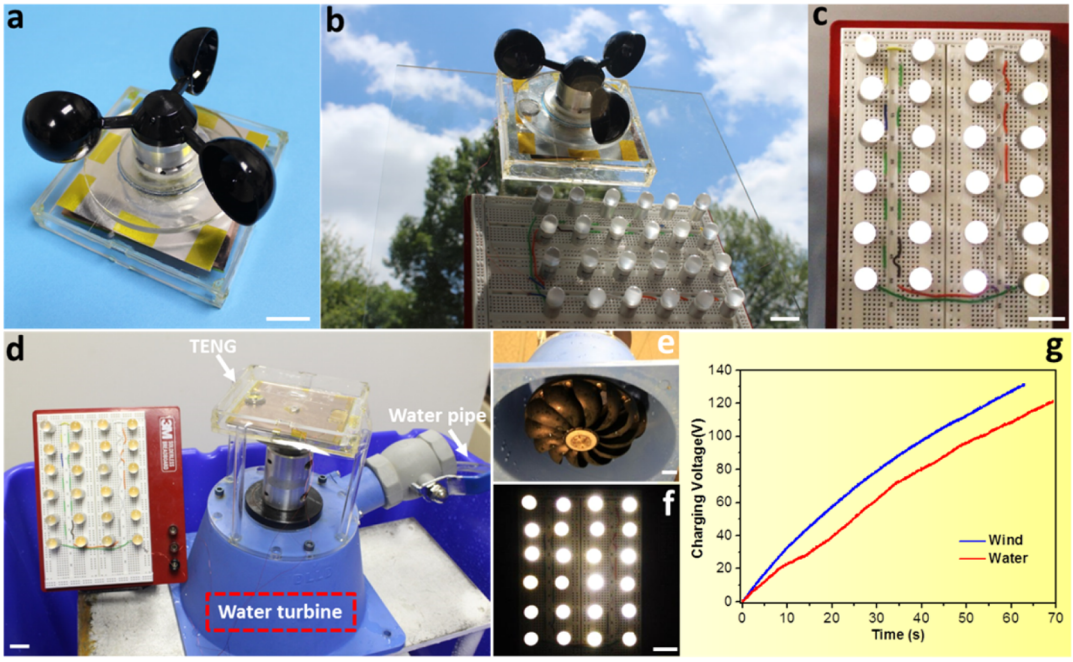

Figure 5. Demonstration of the AT-TENG for harvesting energy from ambient wind and water flow. (a) Photograph of the as-developed AT-TENG-based wind energy harvester. (b) Device in the ambient environment. (c) Harvesting energy from light wind at a flow speed of 6.5 m/s by the AT-TENG, and an array of 24 spot lights was lighted up simultaneously. (d) Harvesting energy from the water flow at a flow rate of 5.5 L/min. (e) Photograph of the upward view of the water turbine. (f) Array of 24 spot lights were lighted up simultaneously. (g) Charging a commercial capacitor when the AT-TENG is driven by the above light wind and water flow. All scale bars are 2 cm.

where Δt is the time lag in seconds between two adjacent peaks in the acquired electric signals, and the traveled distance until this moment can simultaneously be calculated by

$$L = \int_0^t \pi D R_t \mathrm{d}t \tag{5}$$

where R_t and L are the real-time rotation rate in rpm and the traveled distance, respectively, N is the segment number of the AT-TENG, and D is the tire diameter of the moving object. It is worth noting that the self-powered speed or distance measurement does not require a uniform motion of the wheel. It can move at arbitrary time-varying velocities, which renders it a compelling feature for practical application. Figure 6d shows a real-time speedometer realized by Labview programming, and the detailed mathematical calculation is presented in Supporting Information Figure S9. Holding a novel but simple structural design, the ultra-robustness of the AT-TENG promises to have extensive applications in wheel-based transport systems for either energy harvesting or self-powered sensing purposes.

CONCLUSION

To maintain the high output performance without compromising the device robustness, we presented a new methodology by fabricating rational designed AT-TENGs, which achieved a high output performance without compromising the device robustness by, first, converting the in-plane sliding electrification into a contact separation working mode and, second, by creating an automatic transition between a contact working state and a noncontact working state. A greatly reduced surface friction assures drastically improved device robustness. Meanwhile, an intermittent transition into contact state also resolved the awkward predicament of triboelectric charge dissipation in the noncontact free-standing mode, which assures a high electric output. As a demonstration of this methodology, AT-TENGs with one segment and two segments were systematically investigated and certain output trends with increasing segment numbers were derived. The AT-TENG was demonstrated to be a sustainable energy technology and efficiently harnesses various ambient mechanical motions for long-time continuous operations. At a wind speed of 6.5 m/s or a water flow rate of 5.5 L/min, the generated power is capable of simultaneously lighting up 24 spot lights (0.6 W each) connected in series and charging a capacitor to more than 120 V in 60 s. Still, the AT-TENG was also developed to recycle the wasted mechanical energy from human bicycling and normal car motion, and the harvested energy can also be used to light up 104 LEDs simultaneously. In addition, possessing unique output characteristics, the AT-TENG was also developed to be a self-powered speedometer for both real-time rotational speed and traveled distance measurement. With a collection of compelling features as structural simplicity, easy fabrication,

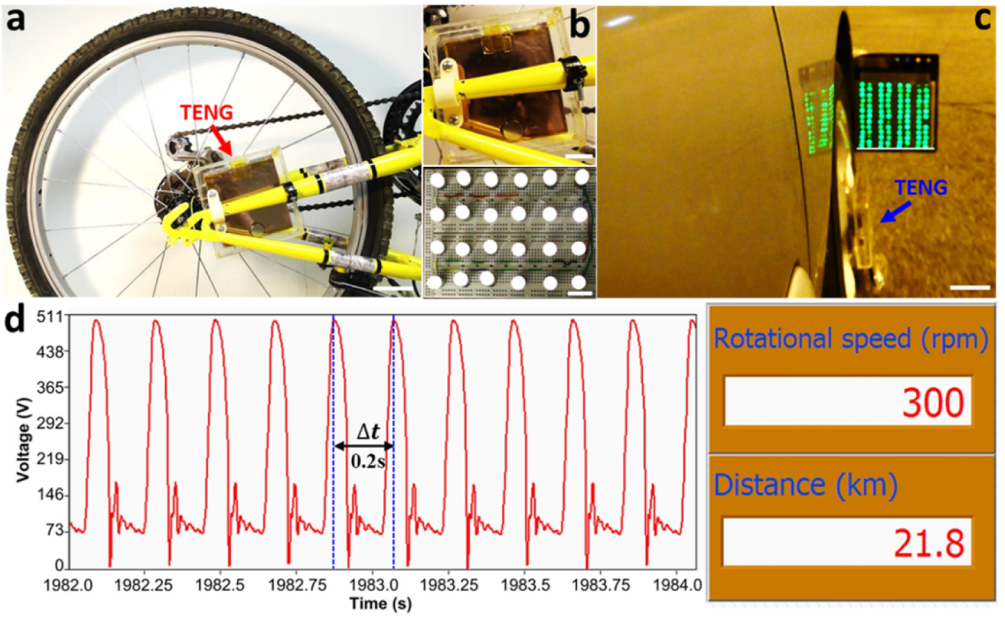

Figure 6. Demonstration of the AT-TENG for recycling mechanical energy from bicycling and a moving car and acting as a self-powered active speedometer. (a) Photograph of the AT-TENG for harvesting energy from bicycling. The scale bar is 5 cm. (b) Top: Enlarged view of the installation of the AT-TENG onto a commercial bike. Bottom: Photograph showing that 24 spot lights were lighted up simultaneously when bicycling naturally. The scale bars are 2 cm. (c) Harvesting energy from a moving car at normal speed, and about 104 LEDs were lighted up simultaneously. The scale bar is 10 cm. (d) Photograph showing the AT-TENG acting as a self-powered active sensor for both real-time moving speed detection and traveled distance measurement.

extremely low cost, wide applicability, and high output performance with superior device robustness, the AT-TENGs presented in this work provide an efficient technology to harvest ambient mechanical motions and are a solid step in the development toward TENG-based self-sustained electronics and systems.

METHODS

Fabrication of Polymer Nanowire Arrays on PTFE Surfaces. First, PTFE thin film with a thickness of 25 μm was cleaned with menthol, isopropyl alcohol, and deionized water and then dried with compressed nitrogen. Second, a layer of 100 nm copper was deposited onto one side of the PTFE film as a back electrode using an electron-beam evaporator. Third, a layer of Au with a thickness of 10 nm was coated onto the other side of the PTFE film as a nanoscale mask. Fourth, Au-coated PTFE was placed into the ICP chamber and then O_2, Ar, and CF_4 gases were introduced into the ICP chamber at flow rates of 10.0, 15.0, and 30.0 sccm, respectively. Fifth, a large density of plasma was generated by a power source of 400 W, and another power source of 100 W was used to accelerate the plasma ions. Finally, the PTFE thin film was etches for 60 s to obtain the polymer nanowires.

Aluminum Nanopore Creation. Using 3% mass fraction oxalic acid ($H_2C_2O_4$) as the electrolyte and a piece of platinum plate as the cathode, an aluminum thin film was electrochemically anodized under a bias voltage of 30 V for 5 h. Then, the alumina layer was etched away in a solution of chromic acid (20 g/L) at 60 °C for 2 h.

Fabrication of an AT-TENG. Acrylic with a thickness of 1.6 mm was cut into dimensions of 10 cm × 10 cm with a laser cutter. On the top layer, the aluminum thin film was laminated onto a piece of the acrylic sheet. On the bottom layer, a nanowire-modified PTFE thin film with deposited copper as the back electrode acted as another contact surface, which was anchored onto the acrylic substrates. Elastic was used to connect one end of the two acrylic sheets with PTFE and aluminum facing each other, leaving another end to stay open. A pair of magnets was adhered onto the open end of the top layer and the rotator plane with a same pole facing each other. Bearings were employed for connection of the rotator plane and functional units.

Experimental Setup for Electrical Measurement. A rotary motor was employed to quantitatively investigate the rotation-rate-dependent electric output of the AT-TENG. The output voltage of the AT-TENG was acquired with a voltage preamplifier (Keithley 6514 system electrometer). The output current of the AT-TENG was acquired by a low-noise current preamplifier (Stanford Research SR560).

Conflict of Interest: The authors declare no competing financial interest.

Acknowledgment. Research was supported by the Hightower Chair foundation, and the "thousands talents" program for pioneer researcher and his innovation team, China. Patents have been filed based on the research results presented in this article.

Supporting Information Available: The Supporting Information is available free of charge on the ACS Publications website at DOI: 10.1021/acsnano.5b05618.

Movie 1 (AVI)
Movie 2 (AVI)
Movie 3 (AVI)
Movie 4 (AVI)
Movie 5 (AVI)
Movie 6 (AVI)
Movie 7 (AVI)
Additional experimental details, equations, and Figures S1–S10 (PDF)

REFERENCES AND NOTES

1. Wang, Z. L. Towards Self-Powered Nanosystems: From Nanogenerators to Nanopiezotronics. *Adv. Funct. Mater.* **2008**, *18*, 3553–3567.

2. Wang, Z. L. Self-Powered Nanosensors and Nanosystems. *Adv. Mater.* **2012**, *24*, 280–285.
3. Wang, Z. L.; Wu, W. Nanotechnology-Enabled Energy Harvesting for Self-Powered Micro-/Nanosystems. *Angew. Chem., Int. Ed.* **2012**, *51*, 11700–11721.
4. Wang, Z. L.; Song, J. Piezoelectric Nanogenerators Based on Zinc Oxide Nanowire Arrays. *Science* **2006**, *312*, 242–246.
5. Xu, S.; Hansen, B. J.; Wang, Z. L. Piezoelectric-Nanowire-Enabled Power Source for Driving Wireless Microelectronics. *Nat. Commun.* **2010**, *1*, 93.
6. Xu, S.; Qin, Y.; Xu, C.; Wei, Y.; Yang, R.; Wang, Z. L. Self-Powered Nanowire Devices. *Nat. Nanotechnol.* **2010**, *5*, 366–373.
7. Yang, R.; Qin, Y.; Dai, L.; Wang, Z. L. Power Generation with Laterally Packaged Piezoelectric Fine Wires. *Nat. Nanotechnol.* **2009**, *4*, 34–39.
8. Zhu, G.; Chen, J.; Zhang, T.; Jing, Q.; Wang, Z. L. Radial-Arrayed Rotary Electrification for High Performance Triboelectric Generator. *Nat. Commun.* **2014**, *5*, 3426.
9. Wang, S.; Lin, L.; Wang, Z. L. Triboelectric Nanogenerators as Self-Powered Active Sensors. *Nano Energy* **2015**, *11*, 436–462.
10. Wang, Z. L.; Chen, J.; Lin, L. Progress in Triboelectric Nanogenertors as A New Energy Technology and Self-Powered Sensors. *Energy Environ. Sci.* **2015**, *8*, 2250–2282.
11. Wang, Z. L. Triboelectric Nanogenerators as New Energy Technology for Self-Powered Systems and as Active Mechanical and Chemical Sensors. *ACS Nano* **2013**, *7*, 9533–9557.
12. Cheng, G.; Lin, Z. H.; Lin, L.; Du, Z. L.; Wang, Z. L. Pulsed Nanogenerator with Huge Instantaneous Output Power Density. *ACS Nano* **2013**, *7*, 7383–7391.
13. Zhu, G.; Peng, B.; Chen, J.; Jing, Q.; Wang, Z. L. Triboelectric Nanogenerators as a New Energy Technology: From Fundamentals, Devices, to Applications. *Nano Energy* **2015**, *14*, 126–138.
14. Cheng, G.; Zheng, L.; Lin, Z. H.; Yang, J.; Du, Z.; Wang, Z. L. Multilayered-Electrode-Based Triboelectric Nanogenerators with Managed Output Voltage and Multifold Enhanced Charge Transport. *Adv. Energy Mater.* **2015**, *5*, 401452.
15. Zhong, J.; Zhong, Q.; Fan, F.; Zhang, Y.; Wang, S.; Hu, B.; Wang, Z. L.; Zhou, J. Finger Typing Driven Triboelectric Nanogenerator and Its Use for Instantaneously Lighting Up LEDs. *Nano Energy* **2013**, *2*, 491–497.
16. Zhu, G.; Chen, J.; Liu, Y.; Bai, P.; Zhou, Y. S.; Jing, Q.; Pan, C.; Wang, Z. L. Linear-Grating Triboelectric Generator Based on Sliding Electrification. *Nano Lett.* **2013**, *13*, 2282–2289.
17. Yang, W.; Chen, J.; Zhu, G.; Yang, J.; Bai, P.; Su, Y.; Jing, Q.; Cao, X.; Wang, Z. L. Harvesting Energy from the Natural Vibration of Human Walking. *ACS Nano* **2013**, *7*, 11317–11324.
18. Yang, J.; Chen, J.; Su, Y.; Jing, Q.; Li, Z.; Yi, F.; Wen, X.; Wang, Z.; Wang, Z. L. Eardrum-Inspired Active Sensors for Self-Powered Cardiovascular System Characterization and Throat-Attached Anti-Interference Voice Recognition. *Adv. Mater.* **2015**, *27*, 1316–1326.
19. Yang, J.; Chen, J.; Liu, Y.; Yang, W.; Su, Y.; Wang, Z. L. Triboelectrification-Based Organic Film Nanogenerator for Acoustic Energy Harvesting and Self-Powered Active Acoustic Sensing. *ACS Nano* **2014**, *8*, 2649–2657.
20. Wen, Z.; Chen, J.; Yeh, M.-H.; Guo, H.; Li, Z.; Fan, X.; Zhang, T.; Zhu, L.; Wang, Z. L. Blow-Driven Triboelectric Nanogenerator as An Active Alcohol Breath Analyzer. *Nano Energy* **2015**, *16*, 38–46.
21. Su, Y.; Zhu, G.; Yang, W.; Yang, J.; Chen, J.; Jing, Q.; Wu, Z.; Jiang, Y.; Wang, Z. L. Triboelectric Sensor for Self-Powered Tracking of Object Motion Inside Tubing. *ACS Nano* **2014**, *8*, 3843–3850.
22. Cheng, G.; Lin, Z. H.; Du, Z.; Wang, Z. L. Increase Output Energy and Operation Frequency of A Triboelectric Nanogenerator by Two Grounded Electrodes Approach. *Adv. Funct. Mater.* **2014**, *24*, 2892–2898.
23. Li, Z.; Chen, J.; Yang, J.; Su, Y.; Fan, X.; Wu, Y.; Yu, C.; Wang, Z. L. β-Cyclodextrin Enhanced Triboelectrification for Self-Powered Phenol Detection and Electrochemical Degradation. *Energy Environ. Sci.* **2015**, *8*, 887–896.
24. Chen, J.; Zhu, G.; Yang, J.; Jing, Q.; Bai, P.; Yang, W.; Qi, X.; Su, Y.; Wang, Z. L. Personalized Keystroke Dynamics for Self-Powered Human–Machine Interfacing. *ACS Nano* **2015**, *9*, 105–116.
25. Cheng, G.; Lin, Z. H.; Du, Z. L.; Wang, Z. L. Simultaneously Harvesting Electrostatic and Mechanical Energies from Flowing Water by a Hybridized Triboelectric Nanogenerator. *ACS Nano* **2014**, *8*, 1932–1939.
26. Fan, X.; Chen, J.; Yang, J.; Bai, P.; Li, Z.; Wang, Z. L. Ultrathin, Rollable, Paper-Based Triboelectric Nanogenerator for Acoustic Energy Harvesting and Self-Powered Sound Recording. *ACS Nano* **2015**, *9*, 4236–4243.
27. Lin, Z. H.; Cheng, G.; Wu, W.; Pradel, K. C.; Wang, Z. L. Dual-Mode Triboelectric Nanogenerator for Harvesting Water Energy and as A Self-Powered Ethanol Nanosensor. *ACS Nano* **2014**, *8*, 6440–6448.
28. Chen, J.; Yang, J.; Li, Z.; Fan, X.; Zi, Y.; Jing, Q.; Guo, H.; Wen, Z.; Pradel, K. C.; Niu, S.; et al. Networks of Triboelectric Nanogenerators for Harvesting Water Wave Energy: A Potential Approach Toward Blue Energy. *ACS Nano* **2015**, *9*, 3324–3331.
29. Zhu, G.; Bai, P.; Chen, J.; Wang, Z. L. Power-Generating Shoe Insole Based on Triboelectric Nanogenerators for Self-Powered Consumer Electronics. *Nano Energy* **2013**, *2*, 688–692.
30. Lin, L.; Xie, Y.; Niu, S.; Wang, S.; Yang, P. K.; Wang, Z. L. Robust Triboelectric Nanogenerator Based on Rolling Electrification and Electrostatic Induction at An Instantaneous Energy Conversion Efficiency of $\sim$ 55%. *ACS Nano* **2015**, *9*, 922–930.
31. Zi, Y.; Lin, L.; Wang, J.; Wang, S.; Chen, J.; Fan, X.; Yang, P. K.; Yi, F.; Wang, Z. L. Triboelectric–Pyroelectric–Piezoelectric Hybrid Cell for High-Efficiency Energy-Harvesting and Self-Powered Sensing. *Adv. Mater.* **2015**, *27*, 2340–2347.
32. Guo, H.; Chen, J.; Yeh, M. H.; Fan, X.; Wen, Z.; Li, Z.; Hu, C.; Wang, Z. L. An Ultrarobust High-Performance Triboelectric Nanogenerator Based on Charge Replenishment. *ACS Nano* **2015**, *9*, 5577–5584.
33. Lin, L.; Wang, S.; Niu, S.; Liu, C.; Xie, Y.; Wang, Z. L. Noncontact Free-Rotating Disk Triboelectric Nanogenerator as A Sustainable Energy Harvester and Self-Powered Mechanical Sensor. *ACS Appl. Mater. Interfaces* **2014**, *6*, 3031–3038.
34. Wang, S.; Xie, Y.; Niu, S.; Lin, L.; Wang, Z. L. Freestanding Triboelectric-Layer-Based Nanogenerators for Harvesting Energy from A Moving Object or Human Motion in Contact and Non-contact Modes. *Adv. Mater.* **2014**, *26*, 2818–2824.
35. Li, S.; Wang, S.; Zi, Y.; Wen, Z.; Lin, L.; Zhang, G.; Wang, Z. L. Largely Improving the Robustness and Lifetime of Triboelectric Nanogenerators Through Automatic Transition Between Contact and Noncontact Working States. *ACS Nano* **2015**, *9*, 7479–7487.
36. Yang, W.; Chen, J.; Jing, Q.; Yang, J.; Wen, X.; Su, Y.; Zhu, G.; Bai, P.; Wang, Z. L. 3D Stack Integrated Triboelectric Nanogenerator for Harvesting Vibration Energy. *Adv. Funct. Mater.* **2014**, *24*, 4090–4096.
37. Fang, H.; Wu, W.; Song, J.; Wang, Z. L. Controlled Growth of Aligned Polymer Nanowires. *J. Phys. Chem. C* **2009**, *113*, 16571–16574.
38. Yang, W.; Chen, J.; Wen, X.; Jing, Q.; Yang, J.; Su, Y.; Zhu, G.; Wu, W.; Wang, Z. L. Triboelectrification Based Motion Sensor for Human-Machine Interfacing. *ACS Appl. Mater. Interfaces* **2014**, *6*, 7479–7484.
39. Yang, W.; Chen, J.; Zhu, G.; Wen, X.; Bai, P.; Su, Y.; Lin, Y.; Wang, Z. L. Harvesting Vibration Energy by A Triple-Cantilever Based Triboelectric Nanogenerator. *Nano Res.* **2013**, *6*, 880–886.
40. Zheng, L.; Lin, Z. H.; Cheng, G.; Wu, W.; Wen, X.; Lee, S.; Wang, Z. L. Silicon-Based Hybrid Cell for Harvesting Solar Energy and Raindrop Electrostatic Energy. *Nano Energy* **2014**, *9*, 291–300.

41. Zheng, L.; Cheng, G.; Chen, J.; Lin, L.; Wang, J.; Liu, Y.; Li, H.; Wang, Z. L. Hybridized Power Panel to Simultaneously Generate Electricity from Sunlight, Rain Drops and Wind Around the Clock. *Adv. Energy Mater.* **2015**, *5*, 1501152.
42. Lin, Z. H.; Cheng, G.; Lee, S.; Pradel, K. C.; Wang, Z. L. Harvesting Water Drop Energy By A Sequential Contact-Electrification and Electrostatic-Induction Process. *Adv. Mater.* **2014**, *26*, 4690–4696.
43. Yang, J.; Chen, J.; Yang, Y.; Zhang, H.; Yang, W.; Bai, P.; Su, Y.; Wang, Z. L. Broadband Vibrational Energy Harvesting Based on A Triboelectric Nanogenerator. *Adv. Energy Mater.* **2014**, *4*, 1301322.
44. Chen, J.; Zhu, G.; Yang, W.; Jing, Q.; Bai, P.; Yang, Y.; Hou, T. C.; Wang, Z. L. Harmonic-Resonator-Based Triboelectric Nanogenerator as A Sustainable Power Source and A Self-Powered Active Vibration Sensor. *Adv. Mater.* **2013**, *25*, 6094–6099.
45. Li, Y.; Cheng, G.; Lin, Z. H.; Yang, J.; Lin, L.; Wang, Z. L. Single-Electrode-Based Rotationary Triboelectric Nanogenerator and Its Applications as Self-Powered Contact Area and Eccentric Angle Sensors. *Nano Energy* **2015**, *11*, 323–332.